Engineering Geology 371 (2026) 108891

Contents lists available at ScienceDirect

Engineering Geology

journal homepage: www.elsevier.com/locate/enggeo

The influence of porosity on the damage induced by freeze-thaw cycles on fracture toughness

Giulia Torsello [a,*], Pooya Hamdi [b], Florian Amann [b,c], Marta Castelli [d], Corrado Fidelibus [e]

[a] Norman B. Keevil Institute of Mining Engineering, The University of British Columbia, Vancouver, Canada
[b] Department of Engineering Geology, Rheinisch-Westfälische Technische Hochschule, Aachen, Germany
[c] Fraunhofer Research Institution for Energy Infrastructures and Geotechnologies IEG, Aachen, Germany
[d] Department of Structural, Geotechnical and Building Engineering, Politecnico di Torino, Torino, Italy
[e] Dipartimento di Ingegneria dell'Innovazione, Università del Salento, Lecce, Italy

ARTICLE INFO

Keywords:
Fracture toughness
Semi-Circular Bending (SCB) test
Freeze-thaw damage
Rock microstructure

ABSTRACT

Freeze-Thaw (FT) cycles can affect rock slope stability in periglacial environments, where temperature fluctuations near 0°C may promote progressive damage in fractured rock masses. It is hypothesized that FT may trigger crack-tip propagation and the failure of rock bridges, thereby reducing rock slope stability. Although FT effects in porous rock have been extensively studied, the response of very low-porosity rocks remains poorly constrained, particularly with respect to fracture toughness. This study investigates the influence of FT cycling on Mode I fracture toughness K_{Ic} and fracture processes in two lithologies with contrasting microstructure: a low-porosity, fine-grained quartzite of an alpine periglacial environment and a higher-porosity, coarser-grained sandstone. Semi-Circular Bending (SCB) tests were conducted on specimens in both their natural state and after 60 FT cycles, performed in an environmental chamber between −12°C and room temperature. The results show that quartzite exhibits a limited, though not negligible (only 1.3%), reduction in K_{Ic} after 60 FT cycles, whereas for the sandstone a 7.2% reduction was observed. Digital Image Correlation (DIC) was used to analyze the Fracture Process Zone (FPZ) development in the quartzite specimens, and post-failure thin sections were examined to characterize fracture paths and microstructural damage. Only minor changes are observed in quartzite, whereas sandstone exhibits increased crack tortuosity and intragranular cracking. These differences highlight the role of porosity, grain size, and microstructural arrangement in controlling FT-induced damage. A simplified linear damage model was applied to estimate the potential long-term evolution of the quartzite fracture toughness after the FT cycles. Despite the limited experimental damage, the result of the model suggests that even low-porosity rocks may experience a significant degradation in years, with potential implications for the long-term stability of rock slopes in periglacial environments.

1. Introduction

The rapid progression of global warming is affecting periglacial regions by increasing ground temperatures, promoting permafrost degradation, and expanding the active layer (Haeberli et al., 1993; Bonnaventure and Lamoureux, 2013; Biskaborn et al., 2019; Smith et al., 2022). In recent decades, several high-altitude areas shifted from continuous permafrost, with permanently frozen ground, to cyclic conditions characterized by temperatures fluctuating around 0°C. These changes induce Freeze-Thaw (FT) cycles in the shallow sub-surface (Matsuoka et al., 1998), which can contribute to degrading slope stability. FT cycles may weaken cohesive bonds along fractures, reduce the strength of rock bridges, and increase the likelihood of rockfalls.

Field observations indicate that FT processes can be linked to increased rockfall activity and permafrost-related mass movements in high-altitude environments (Huggel et al., 2012; Arosio et al., 2013; Paranunzio et al., 2016; Birien et al., 2024; Stoffel et al., 2024). Studies in limestone cliffs in the French Subalpine Ranges and Austrian Alps show a strong correlation between FT cycles and rockfall frequency, particularly in sunlit regions where snow cover and thermal conditions influence the duration of frost-cracking periods (Frayssines and Hantz, 2006; Kellerer-Pirklbauer, 2017). Similarly, an 18-month Light Detection And Ranging (LiDAR) monitoring campaign in Quebec, Canada, demonstrated that winter FT cycles, spring thaw, and intense rainfall significantly increase rockfall occurrence and magnitude (Birien and Gauthier, 2023). Long-term monitoring in the southern

* Corresponding author.
E-mail address: giulia.torsello@ubc.ca (G. Torsello).

https://doi.org/10.1016/j.enggeo.2026.108891
Received 20 January 2026; Received in revised form 31 May 2026; Accepted 10 June 2026
Available online 15 June 2026

Table 1
List of the symbols used and related parameters/variables.

Symbol	Description	Unit
a, w	notch length and width SCB specimen	mm
A_b	water absorption	%
A_{lig}	ligament area	m^2
B, D, H, R	thickness, diameter, height and radius of specimen	mm
COD	crack opening displacement	mm
COD_p	crack opening displacement at peak load	mm
$\overline{COD_p}$	mean crack opening displacement at peak load	mm
COV	coefficient of variation	%
d_g	equivalent grain diameter	mm
G_f	fracture energy	J m^{-2}
IG	intragranular fracture ratio	%
K_I	Mode I stress intensity factor	MPa $m^{1/2}$
K_{Ic}	Mode I static fracture toughness	MPa $m^{1/2}$
$\overline{K_{Ic}}$	mean Mode I static fracture toughness	MPa $m^{1/2}$
LLD	load-line displacement	mm
LLD_p	load-line displacement at peak load	mm
$\overline{LLD_p}$	mean load-line displacement at peak load	mm
m_d	mass of the dry specimen	g
m_s	mass of the saturated specimen	g
m_h	mass of the specimen immersed in water	g
MAAT	Monthly Average Air Temperature	°C
N	number of FT cycles	–
p_0	open porosity	%
P	applied load	N
P_{max}	peak load	N
$\overline{P_{max}}$	mean peak load	N
s	span distance SCB test	mm
SIF	stress intensity factor	MPa $m^{1/2}$
t	time	h
T	temperature	°C
u_x	displacements x direction	mm
v_{COD}	COD velocity	m s^{-1}
W_0	fracture work	J
$\overline{x}$	mean	–
Y'	Mode I dimensionless SIF	–
β	$a/(D/2)$ ratio	–
ϵ_{xx}	strains x direction	–
ρ_b	apparent density	kg m^{-3}
ρ_{rh}	density of water	kg m^{-3}
σ_c	uniaxial compression strength	MPa
σ_x	standard deviation	–
τ	tortuosity	–
χ	damage coefficient	–

Japanese Alps further indicates that rock wall dynamics are primarily influenced by heavy summer rainfall, while FT cycles intensified by rain and snow in other seasons contribute to long-term rock wall retreat (Matsuoka, 2019). These field observations underscore the need to integrate FT effects into rockfall hazard assessments in high-altitude regions (Volkwein et al., 2011; Krautblatter et al., 2013; Noetzli et al., 2024).

According to the rock-ice mechanical model proposed by Krautblatter et al. (2013), a block of a rock mass in a periglacial environment is subjected to gravitational forces and to thrusts generated by water and ice within fractures. Block stability is controlled by the shear strength available along the fracture. This strength is given by ice, ice-rock and rock-rock contacts, and rock bridges, the latter defined as zones of intact rock between the tips of non-persistent discontinuities (Einstein et al., 1983; Dershowitz et al., 2017). Rock bridges exhibit significantly higher shear and tensile strength than persistent fractures and often provide sufficient resistance to maintain rock slope stability (Stead and Eberhardt, 2013; Elmo et al., 2022). However, in periglacial environments, rock bridges may undergo progressive failure due to FT cycling. During freezing, water penetrating the pores, pre-existing microcracks, and fractures expands upon ice formation, generating frost-heaving forces (Tharp, 1987). During thawing, the stress regime within the rock mass is altered (Matsuoka et al., 1998). Seasonal processes can induce thermal stresses, variations in hydraulic pressure, and strength degradation, leading to progressive fracturing (Krautblatter et al., 2013; Draebing and Krautblatter, 2019). In this context, FT cycles play a critical role in rock slope instabilities. Climate warming promotes permafrost thaw progressively exposing rock bridges to FT processes within an expanding active layer. Therefore, an investigation of the mechanisms acting at the tips of non-persistent fractures is required.

In addition to ice segregation and ice wedging (Murton et al., 2006; Duca et al., 2014), FT-induced rock damage is often attributed to volumetric expansion accompanying the water-ice phase transition. This process mainly affects the upper few centimeters of the bedrock surface, where the pores, microcracks, and fractures may contain water or are nearly saturated. Rapid freezing can detach mineral grains and small rock fragments in the active layer. At the microscale (micro to nanometers), microcracking and progressive weakening of intact rock bridges are influenced primarily by pore size, porosity, degree of saturation, mineral composition, and the distribution of pre-existing microcracks (Walder and Hallet, 1985; Matsuoka, 2001). The accumulation of micro damage promotes crack propagation, resulting in rock bridge failure through coalescence (Griffith, 1924; Bost and Pouya, 2017). On a larger scale, ice expansion within water-filled joints can contribute to joint widening and bedrock weakening (Matsuoka and Murton, 2008).

Numerous studies investigated the effects of FT cycles on intact rock properties, including P-wave velocity, porosity, density, tensile strength, and compressive strength across different lithologies (Bayram, 2012; Mutlutürk et al., 2004; Khanlari et al., 2015; Jamshidi, 2021; Momeni et al., 2016; Chen et al., 2021). The influence of pre-existing fractures on FT-induced degradation and fracturing mechanism was also examined (Arosio et al., 2013; Wang et al., 2020; Sun et al., 2023; Chen et al., 2023), and several damage models were proposed to predict FT-induced deterioration (Meng et al., 2021; İnce and Fener, 2016; Wang et al., 2016; Lin et al., 2020).

At the microscale, advanced techniques were used to characterize the FT damage mechanisms and their influence on the evolution of the pore structure. Liu et al. (2019) used Computed Tomography (CT) imaging to generate a 3D pore network model of sandstone specimens, revealing a significant increase in porosity after FT cycling. Jia et al. (2019) combined Scanning Electron Microscopy (SEM) and Nuclear Magnetic Resonance (NMR) to investigate pore water freezing mechanisms and their effects on sandstone microstructure. Chen et al. (2021) linked the degradation of sandstone mechanical properties after FT cycles to an increase in the size of large pores, identified using Acoustic Emission (AE) and Mercury Intrusion Porosimetry (MIP). Park et al. (2015) used CT imaging to examine the microscale pore expansion in diorite, basalt, and tuff subjected to FT cycles, emphasizing the strong lithological dependence of FT damage. Qi et al. (2024) observed reductions in compressive and tensile strength of granite exposed to FT cycles, associated with pore expansion and fracture propagation revealed by SEM analysis. These studies indicate that progressive degradation of the pore structure weakens the effective resistant area of rock bridges, making them more susceptible to crack propagation. Given that fracture toughness is a critical parameter for assessing susceptibility to crack propagation, research efforts focused on understanding its degradation under FT cycles. Wei et al. (2023) and Cao et al. (2020) examined Mode I, Mode II, and Mixed-Mode fracture toughness in sandstone subjected to FT cycles, reporting comparable decreasing trends across all fracture modes. Abdolghanizadeh et al. (2020) reported a similar decrease in Mode I and Mode II fracture toughness of sandstone and an increase in effective porosity. Deng et al. (2021) further proposed a degradation model for Mode I fracture toughness incorporating the influence of FT cycles, temperature fluctuations, rock porosity, strength, and time-dependent pore water migration.

Despite the significant progress made in understanding FT degradation in porous rocks, the response of very low-porosity rocks (less than 1%) remains largely unexplored. Such rocks are often assumed to experience negligible FT-induced damage due to reduced connected porosity and limited potential for ice formation. However, this assumption was seldom experimentally verified, particularly in terms of fracture toughness. Moreover, even if short-term damage may appear minimal, long-term effects may still affect rock mass stability in periglacial environments. To address this gap, this study investigates the influence of FT-induced damage in two lithologies with different microstructure and porosity, focusing on both alterations in intact rock strength and fracture propagation. The experimental framework builds upon the thermal regime observed in quartzite slopes at the Sommeiller Pass (Piedmont, Italy). Long-term temperature monitoring provides a realistic basis for defining representative FT conditions at the rock mass surface. The fracture mechanics response of Etache quartzite, a fine-grained, high-strength, low-porosity metamorphic rock, and Manciano sandstone, a medium-coarse rock with lower strength and higher porosity, was investigated. Mode I (opening) static fracture toughness was assessed using Semi-Circular Bending (SCB) tests, comparing specimens in their natural conditions with specimens exposed to 60 FT cycles reproduced in the environmental chamber. The adopted FT protocol includes a thawing phase in a water bath to ensure continuous water availability during the cycling process. In addition to fracture toughness measurements, Digital Image Correlation (DIC) was used to characterize the evolution of the Fracture Process Zone (FPZ) and crack propagation in quartzite specimens during loading. Post-failure thin-section analyses were also performed to investigate fracture paths and microstructural damage mechanisms in both lithologies. Finally, the experimental results for the Etache quartzite were interpreted in relation to temperature records from Sommeiller Pass, offering a perspective into the implications of FT-induced degradation for the long-term stability of rock masses in periglacial environments.

In Table 1, a list of all symbols and related parameters/variables is reported.

2. Materials and methods

This section describes the procedures adopted for rock sampling and characterization, SCB specimen preparation, FT treatment, fracture toughness testing, DIC, and post-failure thin-section analysis.

2.1. Geological setting of the Etache quartzite

The Sommeiller Pass site (3000 m a.s.l.) is located in the high Susa Valley of the Piedmont Alps, NW Italy (Fig. 1a). Since 2009, weather and permafrost (up to 100 m depth) temperature monitoring stations were established at the Pass (Fig. 1b). Operated by the Piedmont Regional Agency for Environmental Protection (ARPA Piemonte), they are part of the regional monitoring network developed within the European PermaNET project (Coppa et al., 2025). The monitoring stations are located on a flat area near a south-facing rock wall, characterized by high solar exposure and generally limited snow cover. Long-term temperature records highlight that, since 2014, a positive temperature transition has been progressively developing at approximately 60 m depth, suggesting ongoing degradation of the permafrost base (Coppa et al., 2025). The Sommeiller Pass area is mainly composed of Etache quartzites belonging to the Ambin Unit of the Penninic Domain in the Western Alps. The rock mass is characterized by a high degree of fracturing and weathering. Due to limited site accessibility, in situ core drilling was not feasible. Rock blocks were sampled at the toe of the slope (Figs. 1b, c) and subsequently cored in the laboratory (Fig. 1d). As a result, the collected blocks exhibited varying degrees of weathering and alteration, contributing to inherent heterogeneity among the tested specimens.

Petrographic analyses of the Etache quartzite were performed using thin-section microscopy and X-ray Diffraction (XRD) to determine its mineralogical composition. Physical properties were measured, including water absorption A_b (Eq. (1)) following EN 13755:2008, apparent density ρ_b (Eq. (2)), and open porosity p_0 (Eq. (3)) following EN

Table 2
Geometrical characteristics of the quartzite and sandstone SCB specimens compared to the ISRM 2014 prescriptions.

	ISRM prescription	Adopted value
$a/(D/2)$	0.4–0.6	0.43
B	larger than 0.4D or 30 mm	30 mm
D	larger than 10 × grain size or 76 mm	74 mm
s/D	0.5–0.8	0.68
w	≤ 1.5±0.2 mm	1.2 ± 0.3 mm

1936:2007 guidelines. This study focuses on open porosity, defined as the interconnected (open) pores accessible to fluids and gases, whereas total porosity includes both connected and isolated (closed) pores.

Water absorption A_b (%) was determined as:

$$A_b = \frac{m_s - m_d}{m_d} 100 \quad (1)$$

where m_s is the saturated mass and m_d is the dry mass. To ensure that the vast majority of pores were water saturated, the specimen was weighed after 48 h of immersion in water at atmospheric pressure, re-immersed for an additional 24 h, and weighed again. Saturation was considered stable when the difference between two consecutive measurements was <0.1%. The last measurement after 72 h of immersion was taken as the saturated mass m_s.

The apparent density ρ_b (kg m^{-3}), was evaluated as:

$$\rho_b = \frac{m_d}{m_s - m_h} \rho_{rh} \quad (2)$$

where ρ_{rh} is the water density at 20°C (998 kg m^{-3}), and m_h is the mass of the specimen while immersed in water after 24 h of saturation in the evacuation vessel at 2 kPa.

The open porosity p_0 (%) was calculated as:

$$p_0 = \frac{m_s - m_d}{m_s - m_h} 100 \quad (3)$$

Mechanical properties were evaluated through uniaxial compression tests on six cylindrical specimens (D=55 mm, H=110 mm, H/D=2:1), according to ISRM 2018 suggested methods to determine uniaxial compressive strength σ_c.

2.2. The Manciano sandstone

Quarried predominantly in southern Tuscany, Manciano sandstone is widely used as a building stone throughout the region (Rescic et al., 2024). The sandstone was sourced from 30 mm-thick slabs provided by a local stonemason.

Petrographic analyses of the Manciano sandstone were performed using thin-section microscopy to determine its mineralogical composition and X-ray Fluorescence (XRF) to evaluate its elemental composition. Water absorption A_b, apparent density ρ_b, and open porosity p_0 were determined according to Eqs. (1), (2), and (3).

Rock hardness and abrasiveness tests were assessed following the ISRM 1978 suggested methods, while point load strength was determined according to the ISRM 1985 suggested methods to estimate the uniaxial compressive strength σ_c.

2.3. Semi-circular bending specimens

The SCB specimens were prepared following the ISRM 2014 suggested method for determining the Mode I static fracture toughness K_{Ic}. Quartzite samples were core-drilled using diamond drill bits (Figs. 1c, d) and sliced into disks, subdivided into semi-circular specimens using a diamond saw. Notches were made using water jet cutting, with a semi-circular tip (Fig. 2a). In contrast, the sandstone specimens were entirely obtained by water jet cutting from commercially available slabs (Fig. 2b).

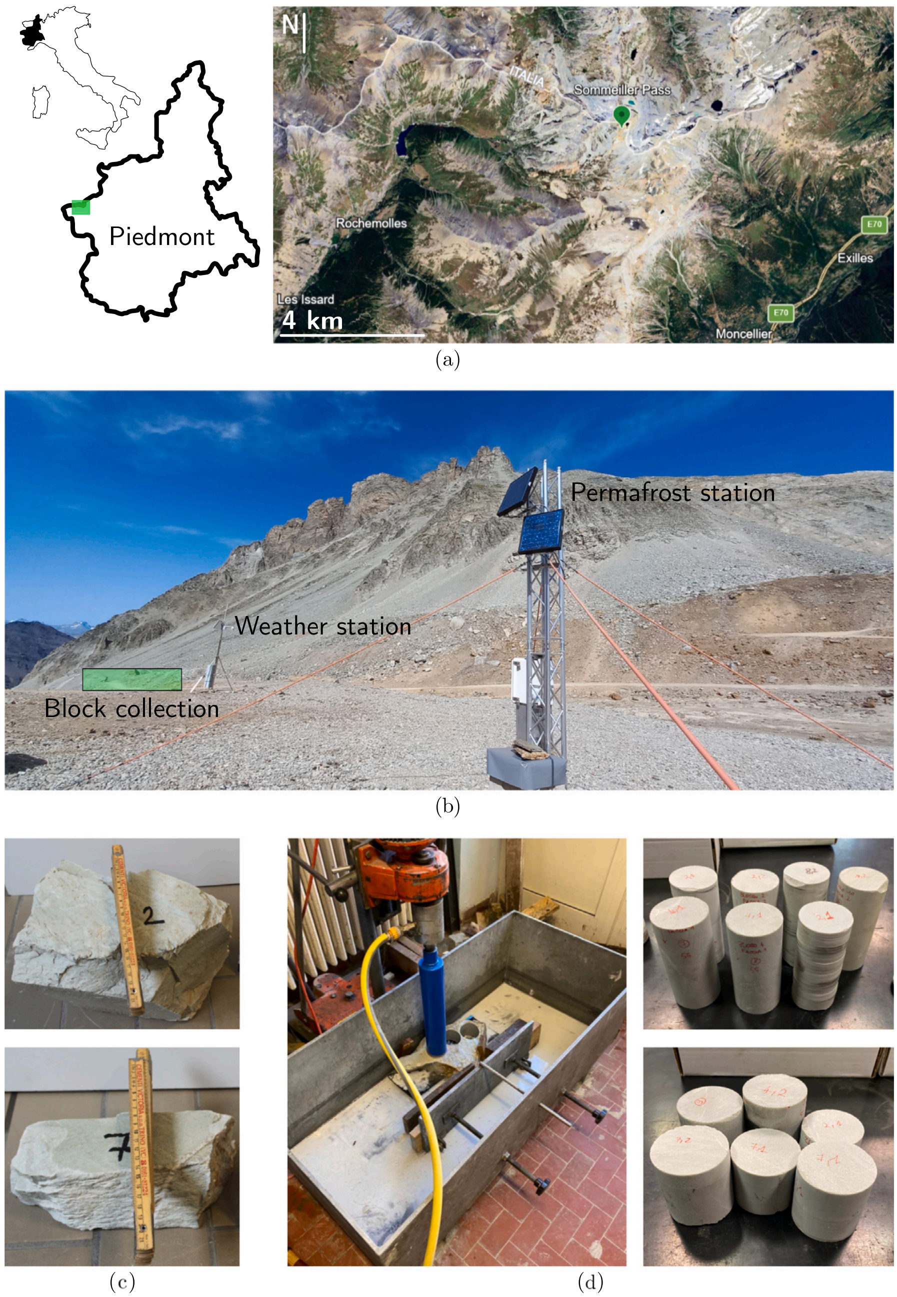

Fig. 1. Sampling site and specimen preparation: (a) location of the Sommeiller Pass site (satellite map from Google Earth); (b) weather and permafrost monitoring stations, with the green area indicating the block collection site; (c) example of collected quartzite blocks used for specimen preparation; (d) fixed core drilling machine and diamond drill bit used to extract some cylindrical specimens from the blocks.

The SCB specimens (Fig. 2c) were prepared with a notch length a=16 mm, thickness B=30 mm, diameter D=74 mm, span distance s=50 mm, and notch width w=1.2 ± 0.3 mm. All dimensions fall within the ranges recommended by ISRM 2014 (Table 2).

2.4. Freezing-Thawing cycles

The SCB testing was performed on 18 quartzite specimens. Nine specimens were tested in the natural state (named 2Nq, 3Nq, 6Nq, 7Nq, 10Nq, 11Nq, 13Nq, 15Nq, 17Nq), and nine specimens were subjected to 60 FT cycles in the environmental chamber (1Dq, 4Dq, 5Dq, 8Dq, 9Dq, 12Dq, 14Dq, 16Dq, 18Dq).

The thermal oscillations adopted during FT cycles were chosen to represent site-specific environmental conditions at the Sommeiller Pass. The applied temperature range represents the thermal regime affecting the rock mass surface and the shallow active layer, and was defined based on Monthly Average Air Temperature (MAAT) data recorded by the weather monitoring station (Fig. 3).

The environmental chamber setup and tank interior with the temperature sensor are shown in Figs. 4a, b. Each FT cycle consisted of a freezing phase followed by thawing (Fig. 4c). Specimens were first cooled in air from room temperature to 0°C at −0.5 ± 0.05°C/min for about 1 h. Below 0°C, the cooling rate was reduced to −0.1 ± 0.05°C/min to allow uniform ice formation, reaching −12°C in about 6 h. Thawing was then performed for 5 h in a water bath at room temperature, ensuring the specimen saturation before the next freezing cycle.

The same procedure was applied to 9 sandstone specimens. Four specimens were tested in the natural state (15Ns, 16Ns, 18Ns, 19Ns), while the remaining five were tested after 60 FT cycles (1Ds, 2Ds, 3Ds,

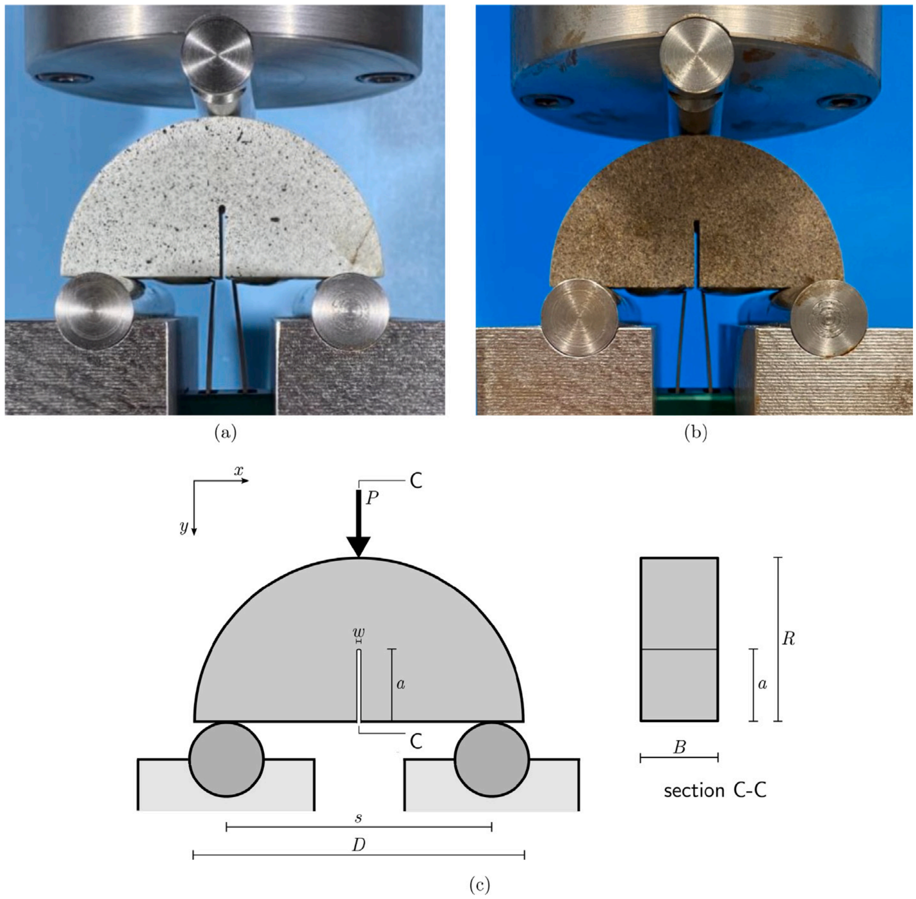

Fig. 2. SCB specimens for Mode I fracture toughness tests: (a) quartzite specimens with black speckles randomly sprayed on the surface for DIC; (b) sandstone specimens both equipped with COD gauges; (c) scheme of the test and section C–C.

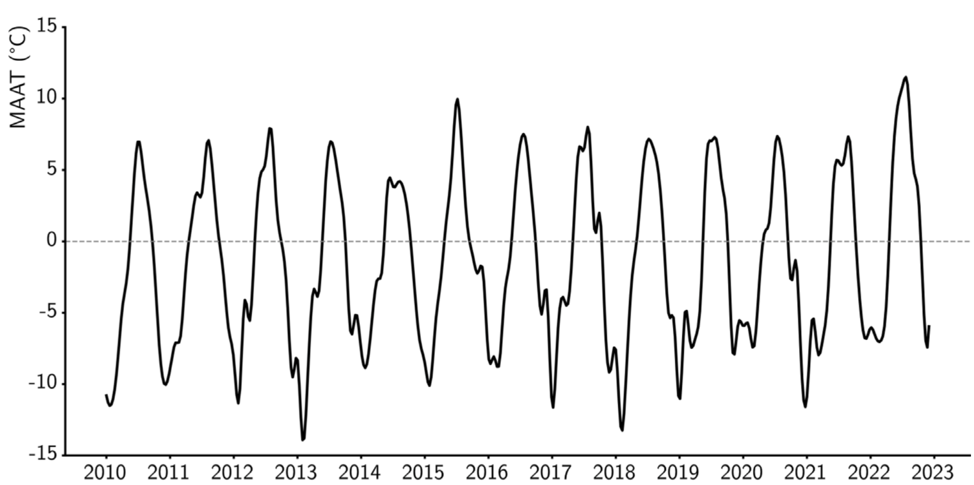

Fig. 3. Monthly Average Air Temperature (MAAT) recorded at the Sommeiller Pass monitoring station (2010–2023).

4Ds, 5Ds), ensuring consistent and comparable FT conditions for both lithologies.

2.5. Fracture toughness

The testing was performed using a ZwickRoell servo-controlled apparatus equipped with a 100 kN load cell to apply a static load P on the specimens, maintaining a constant displacement rate of 0.0125 mm/min. This slow loading rate was chosen to minimize dynamic effects and ensure quasi-static conditions. Load-Line Displacement (LLD) was tracked by LVDTs built into the equipment, and the Crack Opening Displacement (COD) was monitored via an external EPSILON COD gauge.

The Mode I static fracture toughness K_{Ic} using SCB specimens was calculated from the ISRM 2014 suggested methods:

$$K_{\mathrm{Ic}} = Y' \frac{P_{\max}\sqrt{\pi a}}{DB} \tag{4}$$

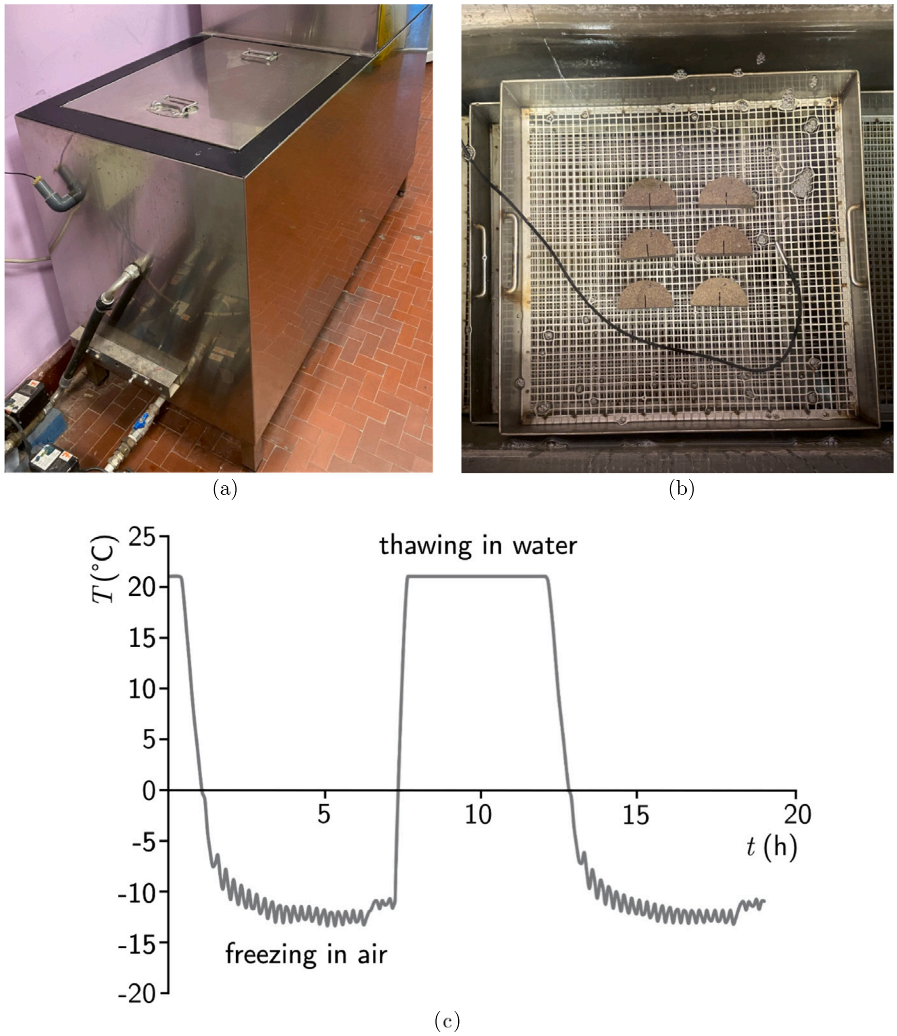

Fig. 4. FT cycles setup: (a) environmental chamber equipped with the tank, pump, and valves for automated control of water inflow and outflow; (b) tank interior filled with water, and temperature sensor positioned near the SCB sandstone specimens; (c) temperatures recorded in the tank plotted against time for a FT cycle.

where $P_{\max}$ is the peak load, and Y' is the Mode I dimensionless Stress Intensity Factor (SIF) obtained from Finite Element Method (FEM) analyses, equal to:

$$Y' = -1.297 + 9.516\frac{s}{D} - \left(0.47 + 16.457\frac{s}{D}\right)\beta + \left(1.071 + 34.401\frac{s}{D}\right)\beta^2 \quad (5)$$

where β is equal to $a/(D/2)$.

2.6. Digital image correlation

DIC was performed on the quartzite specimens to monitor crack initiation and the evolution of the FPZ. The surface of the specimens was sprayed with random black speckle patterns (Fig. 2a), and two white lights were positioned in front of the specimens to ensure uniform image illumination. Data acquired by the ZwickRoell machine and the EPSILON COD gauge were synchronized with the high-speed camera through a common system time reference. Image acquisition was performed using a high-speed camera, the Cyclone-25-150 (Optronis GmbH), capturing at 1000 frames per second (fps), with a frame size of 320 × 300 pixels, and an exposure time of 970 μs. The images were processed using the open-source Ncorr package for MATLAB (Blaber et al., 2015) to obtain displacement and strain maps.

2.7. Post-failure thin sections

Post-failure thin sections of quartzite and sandstone specimens, both in their natural state and after 60 FT cycles, were prepared. Thin sections were taken at the center of the specimens, and were stabilized using blue epoxy resin to enable visualization of the entire fracture propagated from the notch tip. Optical microscopy was utilized to compare the microstructural variance between natural and FT-damaged specimens. The comparison focused on fracture patterns, mineralogical differences, and grain size distribution. Grain size was quantified through the average equivalent grain diameter d_g using ImageJ software (Schneider et al., 2012).

3. Results and interpretation

3.1. Rock properties

The Etache quartzite is a fine-grained metamorphic rock with equivalent grain diameter d_g of 0.1 mm. It is predominantly composed of 90% quartz and 10% mica, with apparent density ρ_b of 2650 kg m^{-3}. The interlocking grain structure is reflected in its very low water absorption (A_b=0.3%) and low open porosity (p_0=0.7%), confirming

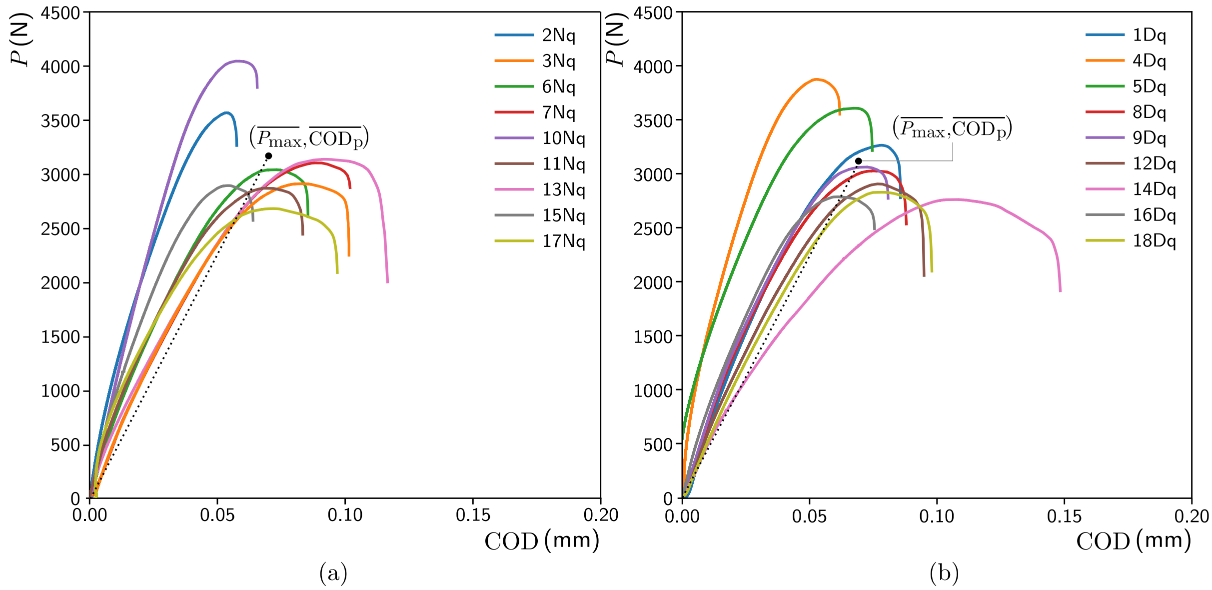

Fig. 5. *P*-COD curves of the quartzite specimens, and equivalent linear elastic curves (dotted); (a) in natural state, (b) pre-damaged after 60 FT cycles.

Table 3
Mean and standard deviation values of the parameters of Etache quartzite and Manciano sandstone.

Rock	d_g (mm)	A_b (%)	ρ_b (kg m^{-3})	p_0 (%)	σ_c (MPa)
quartzite	0.1	0.3 ± 0.1	2650 ± 15	0.7 ± 0.1	192 ± 55
sandstone	0.2	2.3 ± 0.2	2460 ± 14	7.2 ± 0.6	43 ± 5

its classification as a low-porosity rock. This quartzite also exhibits high mechanical strength, with an uniaxial compressive strength σ_c of 192 MPa.

The Manciano sandstone is a medium-coarse sedimentary rock with d_g of 0.2 mm. Its mineralogical composition is more heterogeneous and consists mainly of 30% quartz, 23% calcium, lithic fragments, and minor accessory minerals. The apparent density ρ_b is 2460 kg m^{-3}. Compared to the Etache quartzite, the sandstone exhibits significantly higher open porosity (p_0=7.2%), roughly an order of magnitude greater. Water absorption A_b is 2.3%. The sandstone also has a lower mechanical strength, with an uniaxial compressive strength σ_c of 43 MPa.

The mean values and standard deviations of all measured properties are summarized in Table 3.

3.2. Mode I fracture toughness

Figs. 5 and 6 illustrate the relationship between the load *P* and measured crack opening displacement COD for the quartzite and sandstone specimens, in natural and pre-damaged conditions after 60 FT cycles. Tables 4 and 5 report the corresponding statistical results, including the mean value $\bar{x}$, standard deviation σ_x, and Coefficient Of Variation (COV) of the main parameters: P_{max}, LLD_p, COD_p (i.e., *P*, LLD, COD at peak load), and K_{Ic} derived from Eqs. (4), (5).

As shown in Table 4, the quartzite specimens exhibit similar mean values of $\overline{P_{max}}$ and $\overline{K_{Ic}}$ for both natural and pre-damaged conditions. Likewise, no noticeable differences are observed in the corresponding $\overline{LLD_p}$ and $\overline{COD_p}$ values. The reduction of $\overline{K_{Ic}}$ is limited to 1.3%, signifying that the rock structure did not deteriorate due to the FT cycles. The pronounced variability in the measurements (refer to σ_x and COV) might be attributed to the extraction of the specimens. Quartzite blocks were collected at the toe of the slopes at the Sommeiller Pass area, where superficial fracturing caused by impacts and prolonged exposure to weathering may have induced alterations.

Table 4
Mean, standard deviation, and coefficient of variation of P_{max}, LLD_p, COD_p, K_{Ic} measured with the SCB tests for the Etache quartzite.

		P_{max} (N)	LLD_p (mm)	COD_p (mm)	K_{Ic} (MPa m$^{1/2}$)
natural	$\bar{x}$	3165	0.18	0.07	1.56
	σ_x	440	0.03	0.02	0.22
	COV (%)	14	15	21	14
pre-damaged	$\bar{x}$	3125	0.18	0.07	1.54
	σ_x	390	0.02	0.01	0.17
	COV (%)	12	9	20	11

Table 5
Mean, standard deviation, and coefficient of variation of P_{max}, LLD_p, COD_p, K_{Ic} measured with the SCB tests for the Manciano sandstone.

		P_{max} (N)	LLD_p (mm)	COD_p (mm)	K_{Ic} (MPa m$^{1/2}$)
natural	$\bar{x}$	1590	0.16	0.06	0.83
	σ_x	81	0.02	0.007	0.04
	COV (%)	5	10	24	5
pre-damaged	$\bar{x}$	1475	0.16	0.06	0.77
	σ_x	61	0.02	0.014	0.03
	COV (%)	4	10	13	4

Table 5 summarizes the sandstone results. In contrast to quartzite, the sandstone exhibits a moderate reduction of $\overline{K_{Ic}}$, decreasing by 7.2% after FT cycles. Despite this, no significant changes are noted in the $\overline{LLD_p}$ and $\overline{COD_p}$ values.

The interpretation of SCB tests allows a deeper understanding of the fracture propagation mechanism. The following subsections examine (i) the fracture energy G_f extracted from *P*-COD curve, (ii) the crack growth behavior described by the v_{COD}-K_I kinetic law, and (iii) the FPZ development in quartzite specimens.

3.2.1. Fracture energy

Fracture energy G_f quantifies the energy required to generate new fracture surfaces. Energy is absorbed and released during mechanical loading as microcracks initiate and propagate. Herein G_f (J m^{-2}) up to the peak load is defined as (Bažant, 1996):

$$G_f = \frac{W_0}{A_{lig}} \tag{6}$$

where A_{lig} is the ligament area, calculated as $B(R\text{-}a)$ (Fig. 7a), and W_0 is the fracture work (Fig. 7b). Under Mode I loading, W_0 is obtained

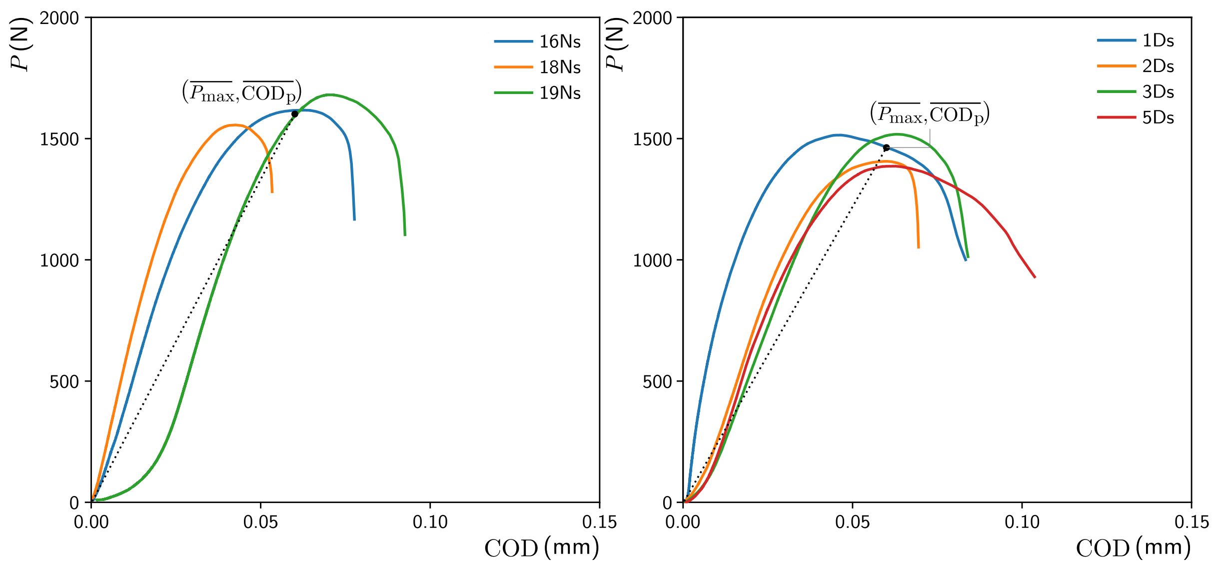

(a) (b)

Fig. 6. P-COD curves of the sandstone specimens, and equivalent linear elastic curves (dotted); (a) in natural state, (b) pre-damaged after 60 FT cycles.

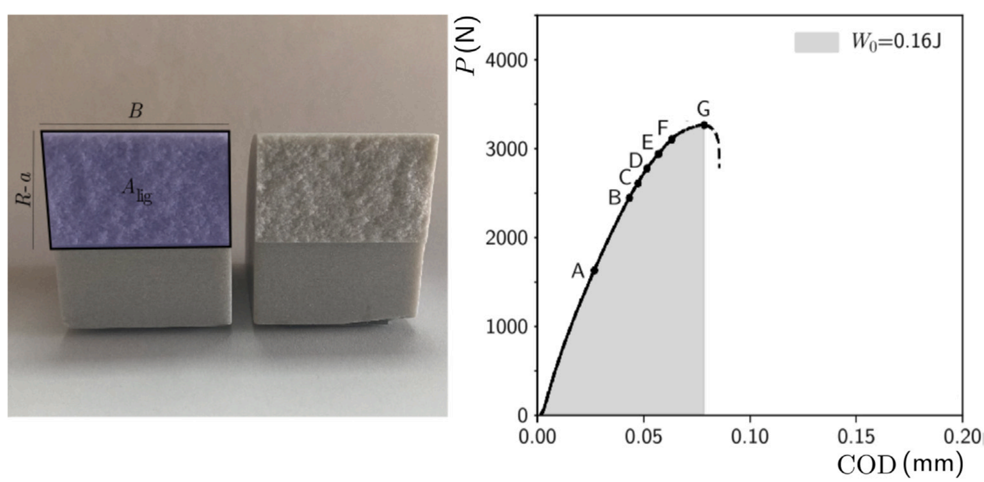

(a) (b)

Fig. 7. Fracture energy G_f components: (a) definition of the ligament area A_{lig}; (b) example of the fracture work W_0 derived from the P-COD curve. Points A-G represent the peak load percentages at which stress intensity factors and crack opening velocity were calculated: A 50%P_{max}, B 75%P_{max}, C 80%P_{max}, D 85%P_{max}, E 90%P_{max}, F 95%P_{max}, G 100%P_{max}.

by integrating the area below the P-COD curve. Specifically, before the peak load, W_0 is expressed as:

$$W_0 = \int_0^{COD_p} P \mathrm{dCOD} \tag{7}$$

where COD_p is the crack opening displacement at peak load, and P is the applied load.

Table 6 summarizes the G_f results for quartzite and sandstone specimens both in natural and pre-damaged conditions, using Eqs. (6), (7). For quartzite, $\overline{G_f}$ changes by only 1.6% between the two states, consistent with the limited variation observed in $\overline{K_{Ic}}$. For sandstone, $\overline{G_f}$ shows a variation of 7.4% after FT cycles, indicating a slight degradation of the rock.

Notably, G_f values differ by one order of magnitude between the two lithologies, with quartzite exhibiting values of about 200 J m^{-2} and sandstone values around 100 J m^{-2}. This difference reflects both the higher strength and the more interlocked microstructure of the quartzite, which requires more energy to generate new fracture surfaces.

Table 6
Mean, standard deviation, and coefficient of variation of G_f for the Etache quartzite and Manciano sandstone.

		G_f (J m^{-2})	
		Quartzite	Sandstone
natural	$\overline{x}$	235.9	95.8
	σ_x	44.2	25.8
	COV (%)	19	27
pre-damaged	$\overline{x}$	232.1	88.7
	σ_x	25.3	8.5
	COV (%)	11	10

3.2.2. Crack growth

The fracture propagation follows a kinetic law, where the time dependency of crack growth is related to the crack velocity v, expressed as a function of the stress intensity factor K at the crack tip (Atkinson,

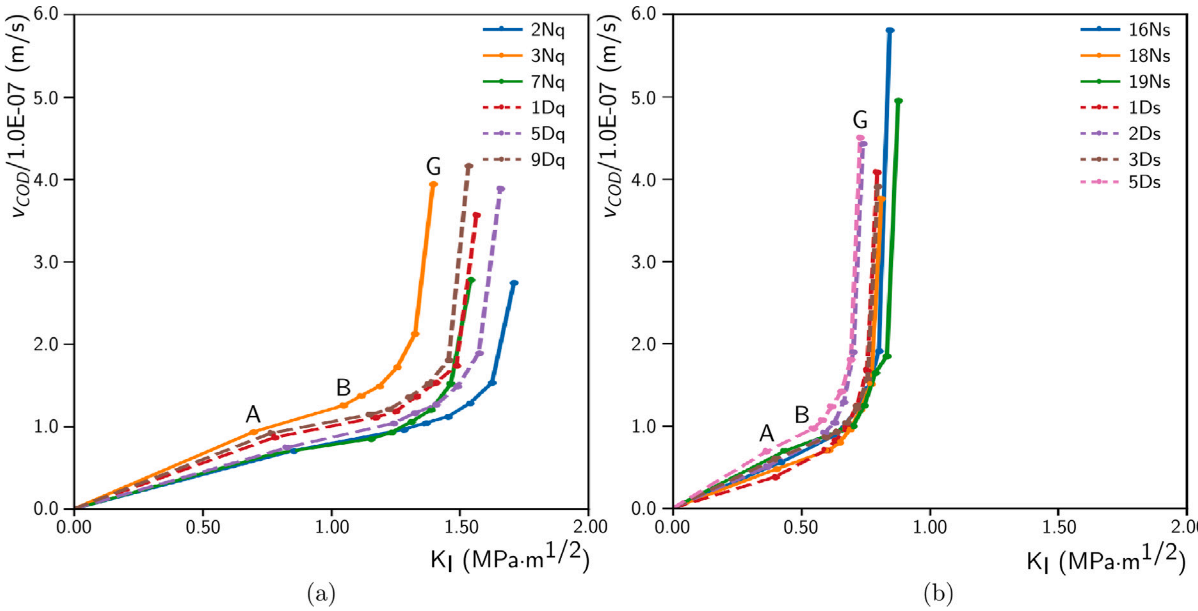

Fig. 8. Selected υ_{COD}-K_{I} curves for (a) quartzite and (b) sandstone specimens both in natural and pre-damaged state.

2015). The typical υ-K curve exhibits three zones capturing the transition from subcritical to dynamic growth: (i) subcritical crack growth, where processes such as stress corrosion at the crack tip drive a steady increase of υ once K exceeds a threshold K_0; (ii) an occasional plateau where υ is approximately constant despite increasing K; (iii) dynamic fracture, in which υ accelerates rapidly as K approaches K_{C}, potentially with unstable propagation and branching.

Some of the experimental υ_{COD}-K_{I} curves obtained for both lithologies are consistent with this general behavior. To track the crack progression, each curve includes seven reference points from A to G, corresponding to crack opening velocity υ_{COD} and stress intensity values K_{I} calculated at fixed percentages of the maximum applied load: 50%, 75%, 80%, 85%, 90%, 95%, and 100% of $P_{\max}$ (reported in Fig. 7b).

Up to point A (50%$P_{\max}$), crack growth is gradual and controlled. In quartzite (Fig. 8a), several specimens display a slight plateau between points A and B, where υ_{COD} temporarily stabilizes. This behavior is not observed in sandstone, where the transition from subcritical crack growth to dynamic propagation appears smoother, with no evident plateau (Fig. 8b). Within the subcritical range, quartzite tends to exhibit lower υ_{COD} than sandstone for a given K_{I}. Point G corresponds to the reached K_{Ic} and marks the onset of unstable propagation.

Regarding the effects of FT damage, the variability observed among the specimens does not allow robust conclusions about its influence on crack velocity.

3.2.3. Fracture Process Zone: Quartzite response

The load-displacement curve used to derive G_{f} also provides important insights into crack growth processes. Specifically, deviations from linearity reveal the onset and progression of microcracking, highlighting how the FPZ develops during loading. The stress field surrounding a crack tip is described by the SIFs, which depend on geometry and boundary conditions. Crack growth is initiated when the SIFs reach the material fracture toughness threshold (Atkinson, 2015). The FPZ forms near the crack tip, and the progression can be depicted in a load-displacement curve (Fig. 9). According to Hoagland et al. (1973), the development is divided into four stages: stage I corresponds to the unloaded conditions, where microdefects are naturally present in the rock, along with additional ones introduced during the notch manufacturing. Random cracks appear with the application of load; stage II, with tensile microcracking generating close to the notch tip while maintaining an elastic response; stage III, involves enhanced microcrack growth ahead of the tip, producing noticeable nonlinearity in the curve; stage IV is marked by the coalescence of microcracks into a new macrocrack and by the extension of the FPZ in front of this newly formed, tension-free crack.

To magnify the evolution of FPZ in quartzite, the response of specimen 1Dq is displayed at points A-G of the P-COD curve in Fig. 7b. The following observations on the four theorized stages are derived from the analysis of Fig. 10.

Stage I

As observed in the DIC strain maps (Fig. 10, maps A-B), the initial stage up to point A is linear, suggesting predominantly elastic behavior of the quartzite. During this phase, microcracking is sparse, and the FPZ starts to develop. At point B, there is minimal horizontal strain ε_{xx}, corroborating the slow crack growth recorded up to 75% of $P_{\max}$ in Fig. 8a.

Stages II and III

By exceeding 75% of $P_{\max}$, the P-COD curve starts to lose linearity, signaling the onset of tensile microcracking near the notch tip and expansion of the FPZ (Fig. 10, maps C-D). The trend is consistent with the dynamic behavior of the υ_{COD}-K_{I} curve expressed in Fig. 8a. Around 90% of $P_{\max}$, significant FPZ development is marked (Fig. 10, map E-F), approaching the critical point near $P_{\max}$. Point G corresponds to 100% of $P_{\max}$, aligning with K_{Ic}. At this stage, the quartzite specimen achieves its peak load capacity; beyond this, it cannot sustain further loads as the FPZ expands permanently (Fig. 11, map G).

Stage IV

Beyond point G, the FPZ reaches its maximum extent, with microcracks coalescing into a larger crack, culminating in complete fracture propagation and specimen failure. After reaching $P_{\max}$, the DIC camera continued capturing images until complete failure of the specimen. Fig. 12 illustrates a frame from the DIC system right before the ultimate failure, highlighting the formation of the macrocrack. This final strain pattern reflects the transition from microcrack accumulation to macrocrack growth, forming a tension-free crack. The displacement field aligns with the splitting stage, illustrating the fracture advancement before the rock divides into two sections.

3.3. Post-failure thin sections

Thin sections were prepared from the central portion of six Etache quartzite specimens (three natural, three pre-damaged) and four sandstone specimens (two natural, two pre-damaged). They were analyzed

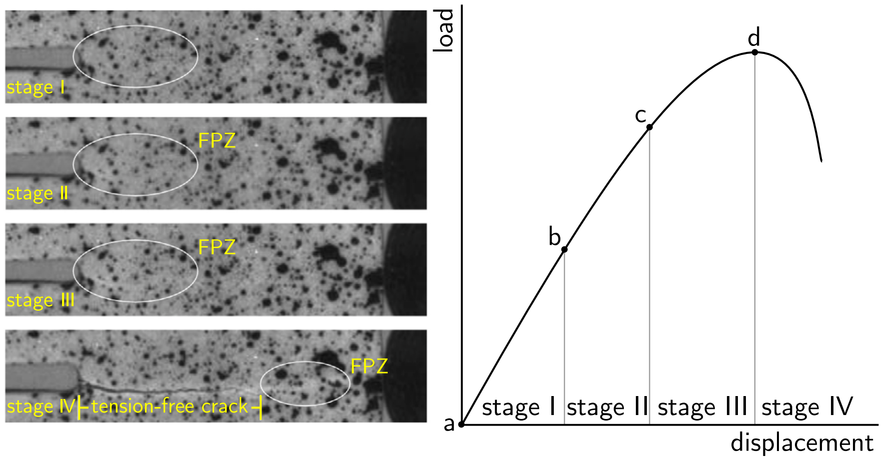

Fig. 9. FPZ development ahead of a crack tip, captured from the frames of the high-speed camera during the tests on the quartzite specimens and typical load versus displacement curve (adapted after Hoagland et al., 1973).

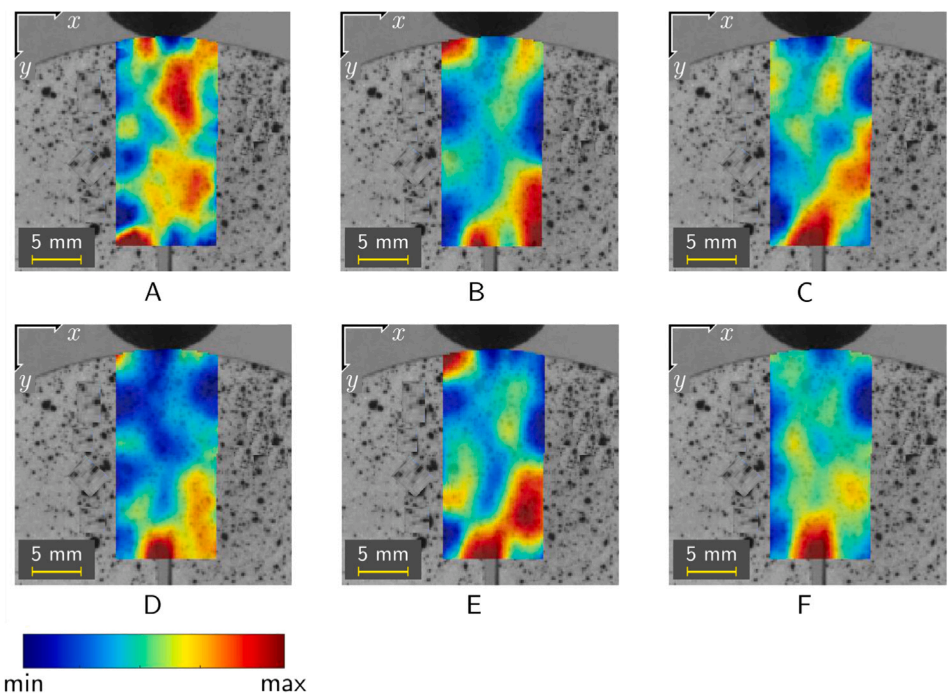

Fig. 10. Maps of the DIC ε_{xx} strains showing the evolution of the fracture from 50% to 95% of P_{max}, corresponding to points A-F on the P-COD curve of Fig. 7b.

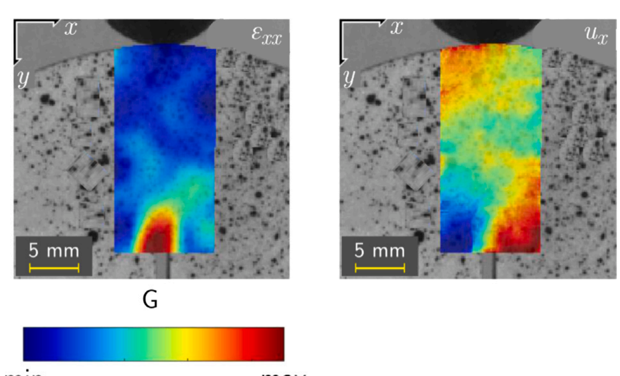

Fig. 11. Maps of the DIC ε_{xx} strains and u_x horizontal displacements showing the evolution of the fracture at 100% of P_{max}, corresponding to point G on the P-COD curve of Fig. 7b.

to quantify fracture tortuosity τ, defined as the ratio of the actual fracture path length to the nominal path length (Chudnovsky and Gorelik, 1996). The Intragranular Fracture ratio (IG) was calculated by dividing the cumulative length of fracture segments crossing mineral grains by the actual fracture path length. In both cases, fracture traces were manually digitized in ImageJ using polyline and analyze tools.

The alignment between the fracture plane and the notch plane was evaluated in the tested specimens after failure. According to the ISRM 2014 suggested methods, Mode I fracture toughness results are invalid if the fracture deviates from the notch plane by more than $0.05D$. For the tested specimens (D=74 mm), the maximum allowable deviation is 3.7 mm. All specimens satisfied this criterion, with fracture paths propagating from the notch toward the loading point without significant deviation, as shown in Fig. 13a.

A quartzite specimen exhibiting the largest deviation (3.1 mm), still within the acceptable tolerance, was included in the analysis for further microstructural investigation. No alternative propagation paths outside the notch direction were observed in this specimen. Thin sections

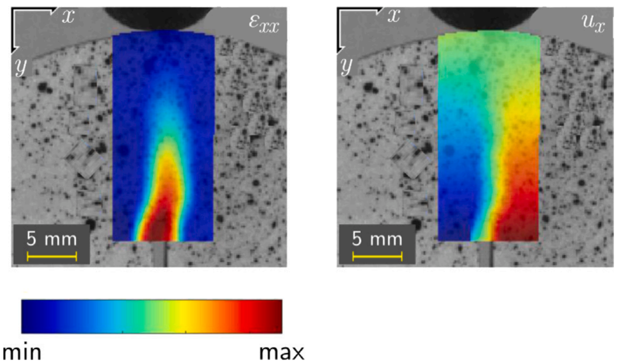

Fig. 12. Maps of the DIC ε_{xx} strains and u_x horizontal displacements showing the evolution of the tension-free crack before complete failure.

revealed a certain microscopic degree of anisotropy in the quartzite, due to mica grains consistently oriented approximately 45° to the loading direction (Fig. 13b). However, no visible interaction between mica grains and fracture paths was observed in the examined specimens. Given the low porosity of quartzite, only minor microstructural changes were observed after FT cycles. The mean τ increased slightly from 1.05 in the natural state to 1.07 in pre-damaged specimens. The variability suggests slight microstructural alterations that might affect crack propagation. IG ratio also rose from 21% to 26%, leading to enhanced fracture propagation through grains rather than along their boundaries after FT cycles.

For sandstone specimens, the mean τ is generally higher than in quartzite, likely due to coarser grain size. Indeed, the mean equivalent diameter d_g is 0.2 mm for sandstone and 0.1 mm for quartzite. The mean τ increased from 1.18 in natural specimens to 1.23 in pre-damaged specimens. The IG ratio was 36.5% in the natural specimens, rising to 39% after FT cycles. Although modest, these variations point to a slightly enhanced FT degradation in the coarser sandstone, highlighting how microstructural features, especially grain size, influence microcrack propagation.

4. Discussion

This study examines the effect of 60 FT cycles on Mode I fracture toughness and fracture processes of two lithologically distinct rocks: a low-porosity, fine-grained quartzite and a higher porosity, coarser sandstone.

In Etache quartzite, K_{Ic} remains largely unchanged after 60 FT cycles. The mean values for natural and pre-damaged specimens are 1.56 MPa $m^{1/2}$ and 1.54 MPa $m^{1/2}$, respectively. This minimal variation confirms that low-porosity, tightly interlocked crystalline rocks are only marginally affected by FT cycling. DIC analysis revealed that the FPZ formation in quartzite remains elastically stable up to 75% of peak load. Beyond this point, localized strain develops at the notch tip, producing unstable crack propagation, consistent with the nonlinear behavior observed in the load-displacement curves.

By contrast, the Manciano sandstone demonstrates a susceptibility to FT cycles, though still moderate. K_{Ic} values for natural and pre-damaged specimens are 0.83 MPa $m^{1/2}$ and 0.77 MPa $m^{1/2}$, respectively.

Furthermore, the mechanical response of the two lithologies differs markedly. On average, sandstone specimens withstand peak loads on the order of 1500 N, whereas quartzite specimens reach peak loads of approximately 3100 N. Despite this large difference, the corresponding LLD and COD values are comparable between the two rocks.

The microstructural analyses mirror these mechanical trends: both rocks display slightly increased fracture tortuosity and a higher proportion of intragranular cracks after FT exposure, but these effects are more pronounced in the coarser-grained sandstone. Overall, the results highlight a link between microstructure, grain size, porosity, and fracture evolution. In some cases, for anisotropic rocks (Dutler et al., 2018), or following treatments such as microwaving (Deyab et al., 2023) or high temperature exposure (Feng et al., 2017), crack propagation under Mode I loading may deviate from the notch plane to follow pre-existing microstructural weaknesses. The quartzite and sandstone investigated in this study exhibited fracture propagation consistently initiating at the notch tip and proceeding along the expected direction. This suggests that, under the investigated FT conditions, fracture propagation remained controlled by notch and loading geometry, with microcrack concentration at the tip of the prefabricated notch, an increase in crack path tortuosity (Yu et al., 2025), and IG ratio.

When compared with published data, the present findings fall within the broader framework of FT-induced degradation as a function of porosity. Literature on sandstone generally reports a reduction of mechanical properties with increasing rock porosity (Deng et al., 2024; Jia et al., 2015; Wei et al., 2023), although the relationship displays substantial scatter due to differences in lithology, FT temperature amplitudes, and number of cycles. The Etache quartzite aligns with other low-porosity rocks, which typically exhibit limited degradation unless exposed to extreme conditions. For instance, a metamorphic quartz-sandstone with 1.01% porosity exhibited no appreciable reduction in uniaxial compression strength even after 105 FT cycles between −40°C and 50°C (Jiang et al., 2019). Similarly, granitoids with porosity below 2% exhibited tensile strength decrease between 13% and 32% only after 300 FT cycles at −30°C, suggesting that significant degradation occurs primarily under extreme conditions of prolonged cycling and low temperatures (Momeni et al., 2016).

To connect the experimentally observed FT damage to the long-term stability of the slopes at the Sommeiller Pass, a preliminary first-order estimate of long-term FT-induced degradation was developed using a simplified linear empirical model describing the evolution of the Etache quartzite K_{Ic} as a function of the number of FT cycles.

The model was validated against the experimental dataset of Wei et al. (2023), where Sichuan sandstone specimens were subjected to 75 FT cycles between −20°C and 20°C. K_{Ic} was measured using Central Cracked Brazilian Disk (CCBD) specimens after 0, 25, 50, and 75 FT cycles.

The linear damage model is expressed as:

$$K_{Ic}(N) = K_{Ic}(0)\,(1 - \chi N) \tag{8}$$

where $K_{Ic}(N)$ is the fracture toughness after N FT cycles, $K_{Ic}(0)$ is the fracture toughness in natural state, and χ is the damage coefficient. Fitting the dataset of Wei et al. (2023) yields χ=0.00224 with R^2=0.99, indicating a good fit.

Considering the relatively high variability of the measured K_{Ic} values, a sensitivity analysis was performed. Nine scenarios were evaluated by combining $\overline{K_{Ic}}\pm\sigma_x$ for both natural and pre-damaged conditions (Table 4). In four cases, K_{Ic} would increase with the number of FT cycles, an outcome physically inconsistent with the microstructural findings. A certain degree of damage occurred in the quartzite specimens, as evidenced by the increase in crack tortuosity and IG ratio. Among the remaining scenarios, the smallest reduction (1.3% after 60 FT cycles) corresponds to the mean values $\overline{K_{Ic}}$ for both natural and pre-damaged conditions. This scenario is therefore prudentially adopted as the reference scenario.

Using $\overline{K_{Ic}(0)}$=1.56 MPa $m^{1/2}$ and $\overline{K_{Ic}(60)}$=1.54 MPa $m^{1/2}$ in Eq. (8), a damage coefficient of χ=0.00021 is obtained. Based on daily air temperature data from 2010–2023, an average of 40 FT cycles per year was identified by counting daily transitions below 0°C. Substituting these values into Eq. (8), the half-life of Etache quartzite K_{Ic} occurs at approximately 2340 FT cycles, corresponding to a timescale of roughly 58.5 years.

The proposed approach should not be interpreted as a predictive tool for quantitative design or stability assessment. Rather, it is intended to qualitatively illustrate how even small variations in fracture

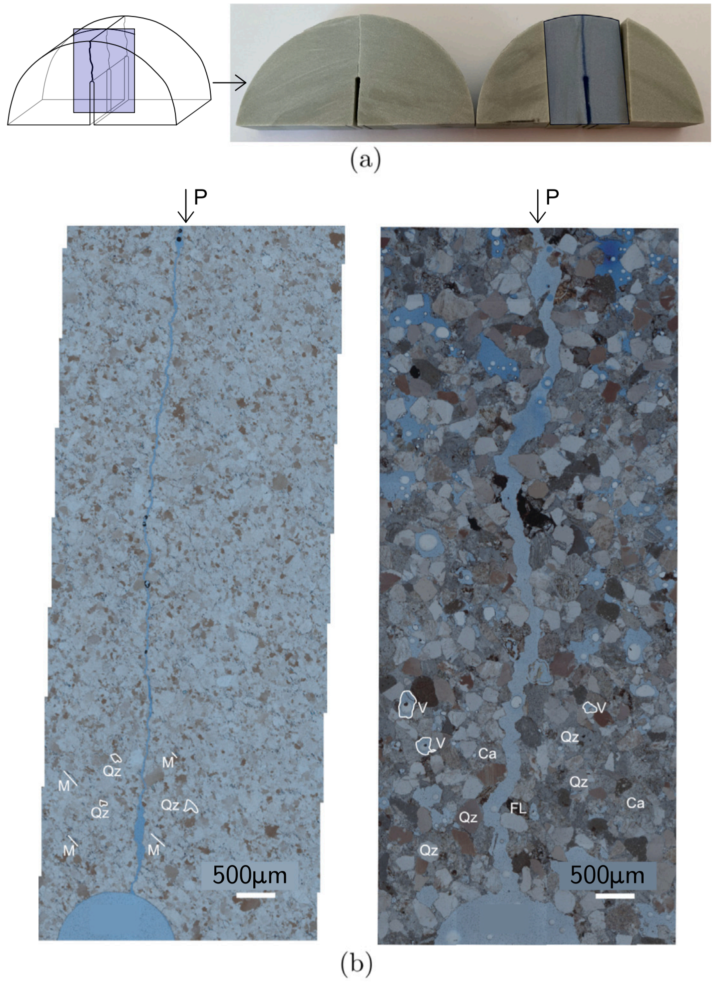

Fig. 13. Microstructural analysis: (a) thin section extraction and representative fracture path; (b) PPL thin sections of the analyzed samples, left: Etache quartzite, primarily composed of quartz (Qz) and mica (M), showing their orientation in relation to the applied load *P*; right: Manciano sandstone, characterized by the presence of quartz (Qz), calcium-rich phases (Ca), voids (V), and lithic fragments (FL). Scale bar: 500 μm.

toughness reduction, associated with a given number of FT cycles, can significantly influence long-term stability. For instance, variations around the reference reduction of 1.3% show that increases to 1.5% and 2% correspond to timescales of about 50 and 37.5 years, respectively (Fig. 14). Conversely, smaller reductions of 1% and 0.5% lead to estimated half-lives of approximately 75 years and 150 years. These results indicate that, although the measured degradation is limited, its cumulative effect over time may still play a significant role in the long-term evolution of rock mass stability under repeated FT cycles.

Several considerations regarding the adopted damage model are necessary. The absence of intermediate measurements between 0 and 60 FT cycles constrains the analysis to a two-point dataset, for which a linear trend represents the only possible interpolation. Despite this limitation, linear trends were reported in the literature for higher numbers of FT cycles, such as the 75 cycles investigated by Wei et al. (2023) and the 80 cycles reported by Yu et al. (2025), supporting the use of a linear approximation as a first-order description. The selection of 60 FT cycles is consistent with both site-specific observations at the Sommeiller Pass and previous studies in alpine environments (Arosio et al., 2013) and was intended to capture the effect of FT processes under representative field conditions. In addition, the site-specific FT count is based on daily temperature fluctuations below 0°C, which provides a simplified representation of the actual and complex thermal regime at the Sommeiller Pass. Further work is required to incorporate intermediate FT cycle gradients, a wider range of cycle numbers, and a more detailed analysis of the thermal fluxes affecting the rock mass.

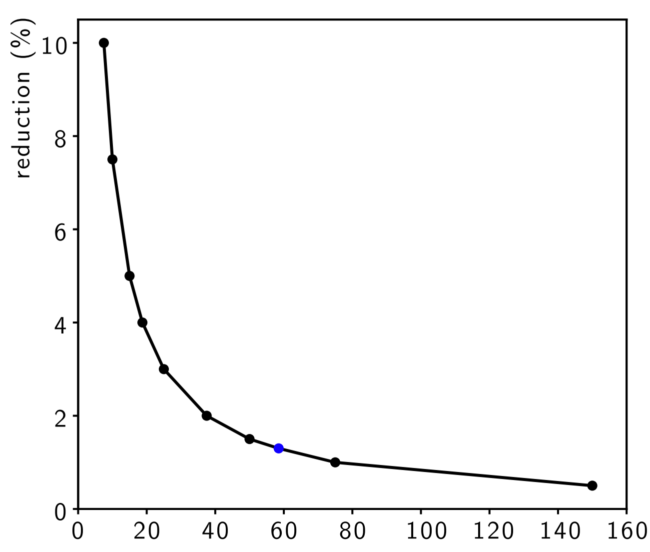

Fig. 14. Sensitivity analysis of FT-induced degradation, showing how different assumed reduction percentages affect the quartzite half-life based on $\overline{K_{Ic}}$. The reference reduction of 1.3% is indicated in blue. (For interpretation of the references to color in this figure legend, the reader is referred to the web version of this article.)

5. Conclusion

This study investigated the FT effects on Mode I fracture toughness and fracture processes of a low-porosity quartzite and a higher-porosity sandstone, integrating mechanical testing, DIC measurements, and microstructural observations. A comparative analysis of the two rock types was conducted to elucidate how differences in porosity affect FT deterioration and fracture toughness, using an experimental FT protocol in which thawing was conducted in a water bath to better reproduce natural conditions in near-surface fractures. Short-term experimental observations were further interpreted using a linear damage model to predict the long-term consequences of FT cycling. Fracture behavior was additionally constrained through microstructural analyses, providing a more comprehensive understanding of how porosity and grain size control rock durability under FT conditions. The main findings are summarized as follows:

- the quartzite showed limited change in fracture toughness after 60 FT cycles, whereas the sandstone exhibited a modest reduction;
- microstructural damage is limited but grain-size and lithology dependent. Both lithologies showed slight increases in fracture tortuosity and intragranular cracking after FT cycling, with larger effects in the coarser and more porous sandstone.

The experimental results can be translated into slope stability metrics through the proposed linear damage model, which provides a preliminary estimate of long-term FT-induced degradation. Applied to the Etache quartzite at the Sommeiller Pass, the model suggests that FT cycling could reduce the fracture toughness to half its initial value within approximately 58.5 years.

In periglacial environments, the increasing occurrence of rockfall events highlights the need to better understand the evolution of fractured rock slopes. A key aspect of this problem is the time-dependent behavior of brittle rocks (Kemeny, 2003), which is rarely accounted for in engineering practice. From the rockfall hazard assessment perspective, as highlighted by Volkwein et al. (2011), hazard assessment should account for temporal dependencies, which requires considering the degradation of rock mass properties under changing environmental conditions. Consequently, the probability of failure should not be considered constant over time. As fracture toughness progressively decreases, the stability of rock bridges is reduced, leading to an increasing likelihood of failure. Incorporating this evolution allows hazard analyses to move from time-independent to time-dependent scenarios. The proposed approach can support qualitative evaluations of failure probability within preliminary and simplified hazard assessments.

The present study also raises open questions regarding the role of time-dependent damage from a design perspective. The results suggest that the use of constant mechanical properties may not adequately represent the long-term behavior of rock masses. In engineered slopes, such as open-pit mines or open excavations exposed to FT cycles, the progressive reduction of fracture toughness may influence the onset of instability and the time of failure. These findings highlight the need to account for time-dependent damage, particularly as environmental conditions continue to evolve.

CRediT authorship contribution statement

Giulia Torsello: Writing – review & editing, Writing – original draft, Visualization, Validation, Methodology, Data curation, Conceptualization. **Pooya Hamdi:** Writing – review & editing, Writing – original draft, Supervision, Methodology, Data curation, Conceptualization. **Florian Amann:** Writing – review & editing, Writing – original draft, Validation, Supervision, Methodology, Conceptualization. **Marta Castelli:** Writing – review & editing, Writing – original draft, Supervision, Funding acquisition, Conceptualization, Project administration. **Corrado Fidelibus:** Writing – review & editing, Writing – original draft, Validation, Supervision, Methodology, Conceptualization.

Fundings

This study was carried out within the RETURN Extended Partnership and received funding from the European Union Next-GenerationEU (National Recovery and Resilience Plan - NRRP, Mission 4, Component 2, Investment 1.3 - D.D. 1243 2/8/2022, PE0000005) - SPOKE VS 2.

Declaration of competing interest

The authors declare that they have no known competing financial interests or personal relationships that could have appeared to influence the work reported in this paper.

Data availability

Data will be made available on request.

References

Abdolghanizadeh, K., Hosseini, M., Saghafiyazdi, M., 2020. Effect of freezing temperature and number of freeze-thaw cycles on mode I and mode II fracture toughness of sandstone. Theor. Appl. Fract. Mech. 105, 102428.
Arosio, D., Longoni, L., Mazza, F., Papini, M., Zanzi, L., 2013. Freeze-thaw cycle and rockfall monitoring. Landslide Sci. Pr.: Vol. 2: Early Warn. Instrum. Monit. 385–390.
Atkinson, B.K., 2015. Fracture Mechanics of Rock. Elsevier.
Bayram, F., 2012. Predicting mechanical strength loss of natural stones after freeze–thaw in cold regions. Cold Reg. Sci. & Technol. 83, 98–102.
Bažant, Z.P., 1996. Analysis of work-of-fracture method for measuring fracture energy of concrete. J. Eng. Mech. 122 (2), 138–144.
Birien, T., Gauthier, F., 2023. Assessing the relationship between weather conditions and rockfall using terrestrial laser scanning to improve risk management. Nat. Hazards Earth Syst. Sci. 23 (1), 343–360.
Birien, T., Gauthier, F., Meloche, F., 2024. Global warming impacts on rockfall frequency and magnitude due to changing frost distribution and frost cracking effectiveness. Earth Surf. Process. Landf..
Biskaborn, B.K., Smith, S.L., Noetzli, J., Matthes, H., Vieira, G., Streletskiy, D.A., Schoeneich, P., Romanovsky, V.E., Lewkowicz, A.G., Abramov, A., et al., 2019. Permafrost is warming at a global scale. Nat. Commun. 10 (1), 264.
Blaber, J., Adair, B., Antoniou, A., 2015. Ncorr: open-source 2D digital image correlation MATLAB software. Exp. Mech. 55 (6), 1105–1122.
Bonnaventure, P.P., Lamoureux, S.F., 2013. The active layer: A conceptual review of monitoring, modelling techniques and changes in a warming climate. Prog. Phys. Geogr. 37 (3), 352–376.
Bost, M., Pouya, A., 2017. Stress generated by the freeze-thaw process in open cracks of rock walls: empirical model for tight limestone. Bull. Eng. Geol. Environ. 76 (4), 1491–1505.
Cao, R., Wang, C., Yao, R., Hu, T., Lei, D., Lin, H., Zhao, Y., 2020. Effects of cyclic freeze-thaw treatments on the fracture characteristics of sandstone under different fracture modes: Laboratory testing. Theor. Appl. Fract. Mech. 109, 102738.
Chen, L., Li, K., Song, G., Zhang, D., Liu, C., 2021. Effect of freeze-thaw cycle on physical and mechanical properties and damage characteristics of sandstone. Sci. Rep. 11 (1), 12315.
Chen, Y., Lin, H., Liang, L., 2023. Freeze-thaw failure characteristics and strength loss of non-penetrating fractured rock mass with different fracture densities. Theor. Appl. Fract. Mech. 124, 103792.
Chudnovsky, A.I., Gorelik, M.L., 1996. Statistical aspects of toughness in brittle fracture. In: Advances in Failure Mechanisms in Brittle Materials. In: ASME International Mechanical Engineering Congress and Exposition, pp. 109–117.
Coppa, G., Sanna, F., Paro, L., Musacchio, C., Merlone, A., 2025. Metrological approach for permafrost temperature measurements. Cold Reg. Sci. & Technol. 229, 104364.
Deng, Z., Zhan, X., Zeng, W., Yang, S., Wu, J., 2021. A degradation model of mode I fracture toughness of rock under freeze-thaw cycles. Theor. Appl. Fract. Mech. 115, 103073.
Deng, Z., Zhang, X., Wang, Z., Min, J., Wei, J., 2024. Analysis of fracture toughness deterioration and instability model of dangerous rock masses under freeze–thaw cycles. Theor. Appl. Fract. Mech. 131, 104398.
Dershowitz, W.S., Finnila, A., Rogers, S., Hamdi, P., Moffitt, K.M., 2017. Step path rock bridge percentage for analysis of slope stability. In: U.S. Rock Mechanics/Geomechanics Symposium, pp. ARMA–2017–1045, vol. 51st U.S. Rock Mechanics/Geomechanics Symposium.
Deyab, S.M., Ahmadihosseini, A., Rafezi, H., Hassani, F., Sasmito, A.P., 2023. Investigating microwave treatment of rocks based on fracture mechanics analysis in mode I fracture toughness test. Rock Mech. Rock Eng. 56 (7), 5275–5291.
Draebing, D., Krautblatter, M., 2019. The efficacy of frost weathering processes in alpine rockwalls. Geophys. Res. Lett. 46 (12), 6516–6524.

Duca, S., Occhiena, C., Mattone, M., Sambuelli, L., Scavia, C., 2014. Feasibility of ice segregation location by acoustic emission detection: A laboratory test in gneiss. Permafr. Periglac. Process. 25 (3), 208–219.
Dutler, N., Nejati, M., Valley, B., Amann, F., Molinari, G., 2018. On the link between fracture toughness, tensile strength, and fracture process zone in anisotropic rocks. Eng. Fract. Mech. 201, 56–79.
Einstein, H., Veneziano, D., Baecher, G., O'Reilly, K., 1983. The effect of discontinuity persistence on rock slope stability. Int. J. Rock Mech. Min. Sci. 20 (5), 227–236.
Elmo, D., Stead, D., Yang, B., Marcato, G., Borgatti, L., 2022. A new approach to characterise the impact of rock bridges in stability analysis. Rock Mech. Rock Eng. 55 (5), 2551–2569.
Feng, G., Kang, Y., Meng, T., Hu, Y.-q., Li, X.-h., 2017. The influence of temperature on mode I fracture toughness and fracture characteristics of sandstone. Rock Mech. Rock Eng. 50 (8), 2007–2019.
Frayssines, M., Hantz, D., 2006. Failure mechanisms and triggering factors in calcareous cliffs of the subalpine ranges (french alps). Eng. Geol. 86 (4), 256–270.
Griffith, A.A., 1924. The theory of rupture. In: International Congress for Applied Mechanics.
Haeberli, W., Guodong, C., Gorbunov, A.P., Harris, S.A., 1993. Mountain permafrost and climatic change. Permafr. Periglac. Process. 4 (2), 165–174.
Hoagland, R.G., Hahn, G.T., Rosenfield, A.R., 1973. Influence of microstructure on fracture propagation in rock. Rock Mech. 5 (2), 77–106.
Huggel, C., Clague, J.J., Korup, O., 2012. Is climate change responsible for changing landslide activity in high mountains? Earth Surf. Process. Landf. 37 (1), 77–91.
İnce, İ., Fener, M., 2016. A prediction model for uniaxial compressive strength of deteriorated pyroclastic rocks due to freeze–thaw cycle. J. Afr. Earth Sci. 120, 134–140.
Jamshidi, A., 2021. Predicting the strength of granitic stones after freeze-thaw cycles: Considering the petrographic characteristics and a new approach using petro-mechanical parameter. Rock Mech. Rock Eng. 54 (6), 2829–2841.
Jia, H., Ding, S., Wang, Y., Zi, F., Sun, Q., Yang, G., 2019. An NMR-based investigation of pore water freezing process in sandstone. Cold Reg. Sci. & Technol. 168, 102893.
Jia, H., Xiang, W., Krautblatter, M., 2015. Quantifying rock fatigue and decreasing compressive and tensile strength after repeated freeze-thaw cycles. Permafr. Periglac. Process. 26 (4), 368–377.
Jiang, Y., Wu, G., Fang, L., 2019. Research on physical and mechanics properties of metamorphic sandstone subjected to freeze-thaw cycles. In: IOP Conference Series: Earth and Environmental Science, vol. 218, (1), IOP Publishing.
Kellerer-Pirklbauer, A., 2017. Potential weathering by freeze-thaw action in alpine rocks in the European alps during a nine year monitoring period. Geomorphology 296, 113–131.
Kemeny, J., 2003. The time-dependent reduction of sliding cohesion due to rock bridges along discontinuities: a fracture mechanics approach. Rock Mech. Rock Eng. 36 (1), 27–38.
Khanlari, G., Sahamieh, R.Z., Abdilor, Y., 2015. The effect of freeze-thaw cycles on physical and mechanical properties of upper red formation sandstones, central part of Iran. Arab. J. Geosci. 8 (8), 5991–6001.
Krautblatter, M., Funk, D., Günzel, F.K., 2013. Why permafrost rocks become unstable: a rock–ice–mechanical model in time and space. Earth Surf. Process. Landf. 38 (8), 876–887.
Lin, H., Lei, D., Yong, R., Jiang, C., Du, S., 2020. Analytical and numerical analysis for frost heaving stress distribution within rock joints under freezing and thawing cycles. Environ. Earth Sci. 79, 1–17.
Liu, B., Ma, Y., Liu, N., Han, Y., Li, D., Deng, H., 2019. Investigation of pore structure changes in mesozoic water-rich sandstone induced by freeze-thaw process under different confining pressures using digital rock technology. Cold Reg. Sci. & Technol. 161, 137–149.
Matsuoka, N., 2001. Microgelivation versus macrogelivation: towards bridging the gap between laboratory and field frost weathering. Permafr. Periglac. Process. 12 (3), 299–313.
Matsuoka, N., 2019. A multi-method monitoring of timing, magnitude and origin of rockfall activity in the Japanese alps. Geomorphology 336, 65–76.
Matsuoka, N., Hirakawa, K., Watanabe, T., Haeberli, W., Keller, F., 1998. The role of diurnal, annual and millennial freeze-thaw cycles in controlling alpine slope instability. In: Proceedings of the Seventh International Conference on Permafrost. Centre D'Etudes Nordiques, Universite Laval. pp. 711–718.
Matsuoka, N., Murton, J., 2008. Frost weathering: Recent advances and future directions. Permafr. Periglac. Process. 19 (2), 195–210.
Meng, X., Zhang, H., Liu, X., 2021. Rock damage constitutive model based on the modified logistic equation under freeze-thaw and load conditions. J. Cold Reg. Eng. 35 (4), 04021016.
Momeni, A., Abdilor, Y., Khanlari, G., Heidari, M., Sepahi, A., 2016. The effect of freeze–thaw cycles on physical and mechanical properties of granitoid hard rocks. Bull. Eng. Geol. Environ. 75, 1649–1656.
Murton, J.B., Peterson, R., Ozouf, J.-C., 2006. Bedrock fracture by ice segregation in cold regions. Science 314 (5802), 1127–1129.
Mutlutürk, M., Altindag, R., Türk, G., 2004. A decay function model for the integrity loss of rock when subjected to recurrent cycles of freezing–thawing and heating–cooling. Int. J. Rock Mech. Min. Sci. 41 (2), 237–244.
Noetzli, J., Isaksen, K., Barnett, J., Christiansen, H.H., Delaloye, R., Etzelmüller, B., Farinotti, D., Gallemann, T., Guglielmin, M., Hauck, C., et al., 2024. Enhanced warming of European mountain permafrost in the early 21st century. Nat. Commun. 15 (1), 1–15.
Paranunzio, R., Laio, F., Chiarle, M., Nigrelli, G., Guzzetti, F., 2016. Climate anomalies associated with the occurrence of rockfalls at high-elevation in the Italian alps. Nat. Hazards Earth Syst. Sci. 16 (9), 2085–2106.
Park, J., Hyun, C.-U., Park, H.-D., 2015. Changes in microstructure and physical properties of rocks caused by artificial freeze–thaw action. Bull. Eng. Geol. Environ. 74, 555–565.
Qi, L., Wang, J., Zhang, D., Zhang, Y., Ma, J., 2024. Evaluation of the influence of freeze–thaw cycles on the joint strength of granite in the eastern tibetan plateau, China. Sci. Rep. 14 (1), 24085.
Rescic, S., Fratini, F., Sacchi, B., Mattone, M., 2024. The manciano sandstone in contemporary architecture: Conservation aspects in florence. Geoheritage 16 (4), 114.
Schneider, C.A., Rasband, W.S., Eliceiri, K.W., 2012. NIH Image to ImageJ: 25 years of image analysis. Nature Methods 9 (7), 671–675.
Smith, S.L., O'Neill, H.B., Isaksen, K., Noetzli, J., Romanovsky, V.E., 2022. The changing thermal state of permafrost. Nat. Rev. Earth Environ. 3 (1), 10–23.
Stead, D., Eberhardt, E., 2013. Understanding the mechanics of large landslides. Ital. J. Eng. Geol. Environ. 6, 85–112.
Stoffel, M., Trappmann, D.G., Coullie, M.I., Ballesteros Cánovas, J.A., Corona, C., 2024. Rockfall from an increasingly unstable mountain slope driven by climate warming. Nat. Geosci. 17 (3), 249–254.
Sun, L., Tao, S., Liu, Q., 2023. Frost crack propagation and interaction in fissured rocks subjected to freeze–thaw cycles: experimental and numerical studies. Rock Mech. Rock Eng. 56 (2), 1077–1097.
Tharp, T.M., 1987. Conditions for crack propagation by frost wedging. Geol. Soc. Am. Bull. 99 (1), 94–102.
Volkwein, A., Schellenberg, K., Labiouse, V., Agliardi, F., Berger, F., Bourrier, F., Dorren, L.K., Gerber, W., Jaboyedoff, M., 2011. Rockfall characterisation and structural protection: A review. Nat. Hazards Earth Syst. Sci. 11 (9), 2617–2651.
Walder, J., Hallet, B., 1985. A theoretical model of the fracture of rock during freezing. Geol. Soc. Am. Bull. 96 (3), 336–346.
Wang, Y., Feng, W., Wang, H., Li, C., Hou, Z., 2020. Rock bridge fracturing characteristics in granite induced by freeze-thaw and uniaxial deformation revealed by AE monitoring and post-test CT scanning. Cold Reg. Sci. & Technol. 177, 103115.
Wang, P., Xu, J., Liu, S., Liu, S., Wang, H., 2016. A prediction model for the dynamic mechanical degradation of sedimentary rock after a long-term freeze-thaw weathering: Considering the strain-rate effect. Cold Reg. Sci. & Technol. 131, 16–23.
Wei, M., Qiao, L., Li, Q., Deng, N., 2023. On the decay of fracture toughness of sandstone subjected to freeze–thaw cycles. Fatigue Fract. Eng. Mater. Struct. 46 (12), 4465–4485.
Yu, M., Wang, Z., Ma, D., Ge, J., Wang, Y., Xie, H., Wu, G., Meng, Y., 2025. Fracture characteristics and process zone evolution in sandstone under freeze-thaw cycles. Res. Cold Arid. Reg..